Energy & Environmental Science

PAPER

View Article Online
View Journal | View Issue

Cite this: *Energy Environ. Sci.*, 2019, **12**, 1950

Towards membrane-electrode assembly systems for CO_2 reduction: a modeling study†

Lien-Chun Weng,[ab] Alexis T. Bell *[ab] and Adam Z. Weber *[a]

Received 20th March 2019,
Accepted 7th May 2019

DOI: 10.1039/c9ee00909d

rsc.li/ees

Membrane-electrode assemblies (MEAs) are an attractive cell design for the electrochemical reduction of CO_2 because they exhibit low ohmic loss and high energy efficiency. We describe here the development and application of a multiphysics model to investigate the fundamental limitations of two MEA designs: one with gaseous feeds at both the anode and cathode (full-MEA), and the other with an aqueous anode feed ($KHCO_3$ or KOH exchange solution) and a gaseous cathode feed (exchange-MEA). The total current density for the three cases follows the order: KOH-MEA > $KHCO_3$-MEA > full-MEA. This trend is established by examining the distribution of the applied voltage. We show that the main charge-carrying species are carbonate anions for an MEA that uses an anion-exchange membrane (AEM). The amount of CO_2 consumed but not converted to CO decreases with increasing current densities above 100 mA cm^{-2} for a full-MEA, but converges to 50% for exchange-MEAs. The full-MEA becomes limited by ohmic resistance as the membrane dehydrates with increasing cell temperature, and eventually becomes limited due to water mass transport. The exchange-MEAs can maintain membrane hydration and the local ion concentration at the anode, but are limited by salt precipitation at the cathode, as well as a higher tendency to flood. Finally, we explore the effects of temperature and discuss the possibility of increasing water supply to the full-MEA to improve its performance at elevated temperatures. The MEA model and the understanding of MEA performance for the electrochemical reduction of CO_2 presented in this study should help guide the design of next-generation CO_2 reduction cells.

Broader context

CO_2 electrolyzers powered by solar energy, either directly or indirectly, have become increasingly attractive as solar prices decline and atmospheric CO_2 levels rise. The product formed by CO_2 reduction can be used as fuel or as precursors to fuel or chemical industry, thereby enabling the storage of intermittent solar radiation in chemical bonds. For CO_2 electrolyzers to be commercially viable, high current densities must be achieved with good selectivity at relatively low power inputs. The design and optimization of such devices require understanding the underlying physics, which includes transport phenomena, electrochemistry, heat transfer, and reaction kinetics. The work presented here describes a numerical model that accounts for the aforementioned physical phenomena occurring in membrane electrode assemblies (MEAs). The model reveals intrinsic tradeoffs and limitations of MEAs for the electrochemical reduction of CO_2, and establishes design and operating criteria for such systems. The model also confirms that ohmic losses in MEAs are low because charge transport through a liquid electrolyte is eliminated.

Introduction

Electrochemical reduction of CO_2 allows conversion of this greenhouse gas to value-added products under mild conditions. This process also provides a way to store excess electrical energy and tackle intermittency issues associated with renewable energy sources (*e.g.*, wind and solar).[1,2] For the electrochemical reduction of CO_2 to be commercially viable, it is necessary to carry out CO_2 reduction (CO_2R) at current densities >100 mA cm^{-2}, while minimizing the power input (or cell voltage).[3] Such current densities require higher local concentrations of CO_2, which have been achieved predominantly with gas-diffusion electrodes (GDEs), architectures that allow for new avenues of exploration and efficiency.[4] GDEs overcome the significant mass-transfer resistances associated with CO_2R carried out in aqueous electrolytes—a consequence of the large mass-transfer boundary layer near the planar electrodes.[5–13]

Minimizing cell ohmic overpotential requires increasing the conductivity of the electrolyte, and decreasing the distance

[a] *Joint Center for Artificial Photosynthesis, LBNL, Berkeley, CA 94720, USA. E-mail: alexbell@berkeley.edu, azweber@lbl.gov*
[b] *Department of Chemical and Biomolecular Engineering, UC Berkeley, Berkeley, CA 94720, USA*

† Electronic supplementary information (ESI) available. See DOI: 10.1039/c9ee00909d

between the anode and cathode. Membrane-electrode-assemblies (MEAs) satisfy these two requirements by removing the aqueous electrolyte compartments between the electrodes and utilizing an ion-conducting polymer (ionomer) as both the separator and electrolyte. Membranes used in electrochemical systems are typically on the order of 10 to 100 μm thick, with conductivities ranging from 10 to 200 mS cm^{-1}.[14]

There have been numerous reports demonstrating the feasibility of MEA-like cells attaining CO_2R current densities upwards of 100 mA cm^{-2}, an order of magnitude higher than can be achieved using typical aqueous architectures.[5–11,15] Various configurations and materials have been presented, with much debate as to which design is the most effective for scale-up and commercialization, as reviewed[13] and discussed[4] recently. Cook *et al.* first illustrated the electrochemical reduction of CO_2 to hydrocarbons in an MEA design, showing an approximately 0.5 V reduction in the cell potential at 10 mA cm^{-2} when removing the anolyte compartment.[16] Hori *et al.* found that an anion-exchange membrane (AEM) is more suitable for CO_2R than a cation-exchange membrane (CEM), as the CEM not only prevents transport of HCO_3^- and $CO_3^{=}$ anions, but also allows high proton concentrations that promote the competing hydrogen evolution reaction (HER).[17] In agreement with Hori *et al.*, Delacourt *et al.* noted the importance of minimizing proton concentration near the cathode to suppress HER. However, these authors did not observe CO_2R products over Ag using a CEM, but obtained an 80% CO_2R faradaic efficiency (FE) after adding a $KHCO_3$ buffer layer between the cathode and CEM. They found a FE of only 3% for CO_2R with an AEM but did not fully explain why the efficiency was so low.[18] It is notable that Salvatore *et al.* also explored adding a buffer layer between the cathode and membrane to improve the CO_2R current efficiency for an MEA-like cell (aqueous anode feed and gaseous cathode feed, with no anolyte or catholyte compartments). These authors found that the buffer layer provided better hydration, since adding a water layer in place of the buffer layer also achieved a higher CO_2R FE than could be reached in the absence of such a layer.[19] While it is tempting to draw general conclusions from the above studies, it is important to note that each one was performed using cell designs that differed from each other. Hori *et al.* retained the aqueous anolyte compartment but removed the aqueous catholyte compartment;[17] Narayanan, Li, and Salvatore removed the aqueous electrolyte compartments and used an aqueous feed instead;[19–21] and Delacourt, Kriescher, and Wang utilized pure gaseous feeds with no aqueous electrolyte.[18,22,23] Without a quantitative understanding of the limitations of each design, it is difficult to compare the results reported in different studies and to draw general conclusions from them. To date, there has been limited analysis of an MEA performing CO_2R in the absence of aqueous electrolyte compartments at low temperature (as opposed to solid-oxide electrolyzers[24,25]). Delacourt *et al.* simulated an electrochemical cell with a cation exchange membrane and a catholyte (no anolyte), and briefly mentioned replacing the catholyte with an anion-exchange membrane to obtain a higher current density. They concluded that a fully solid-state MEA could enhance performance of a CO_2 electrolyzer, but did not go into details to describe MEA operation and limitations.

In this paper, we present a modeling framework that describes mass transport, electrochemical and homogenous reaction kinetics, and thermal effects for an AEM-MEA cell with pure gaseous feeds (full-MEA), and with a gaseous cathode feed but an aqueous anode feed (exchange-MEA). Our model differs from that for an alkaline fuel-cell/electrolyzer in two main aspects. First, there are competing electrochemical reactions occurring at the cathode (HER and CO_2R) and second, the CO_2 concentration is much higher in the CO_2R system (compared to a maximum of 400 ppm for fuel cell systems), which means that the homogeneous acid/base bicarbonate reactions are significant and must be accounted for, especially in an alkaline environment. We use our model to examine the performance of an MEA system for the CO_2 reduction over an Ag catalyst, which primarily produces CO and H_2. Based on our simulations, we discuss the advantages and limitations of different MEA cell designs for performing CO_2R, and examine potential methods for improving water management in the membrane and the overall cell efficiency. Finally, the presented model, methodology, and subsequent analysis provides a framework for investigating these and related electrochemical energy-conversion processes that involve complex and multiple reaction and transport processes.

Model development

This section aims to discuss the modeling approach, governing equations, and assumptions to give the reader a primer and methodology for tackling complex multiphysics problems common for electrochemical energy-devices. The discussion includes justifications, governing equation formulation, and determination of key parameter values. The MEA model comprises a 50 μm anion-exchange membrane (AEM), a 5 μm Ag cathode catalyst layer (CL), and a 100 μm cathode diffusion medium (DM), as shown in Fig. 1. The anode, an IrO_2 mesh pressed against the membrane, is treated as an interface. N_2 with 100% relative humidity (RH) is fed to the anode chamber for the full-MEA, and an aqueous solution is fed for the exchange-MEA; humidified CO_2 (100% RH) is fed to the cathode chamber for both MEA configurations.

At the anode, the oxygen evolution reaction (OER) occurs *via* both acidic and alkaline processes,

$$2H_2O \rightarrow O_2 + 4H^+ + 4e^- \quad (1)$$

$$4OH^- \rightarrow O_2 + 2H_2O + 4e^- \quad (2)$$

HER and CO_2R reaction occur at the cathode. Similar to the OER, both acidic and alkaline HER can occur,

$$2H^+ + 2e^- \rightarrow H_2 \quad (3)$$

$$2H_2O + 2e^- \rightarrow H_2 + 2OH^- \quad (4)$$

For a Ag cathode, CO has been shown to be the predominant CO_2R product formed, therefore, CO evolution reaction (COER) is equivalent to CO_2R reaction for our system.[10,26,27] Shen *et al.* have observed a less prominent pH-dependence of the COER compared to the HER at low pH, suggesting that H_2O serves

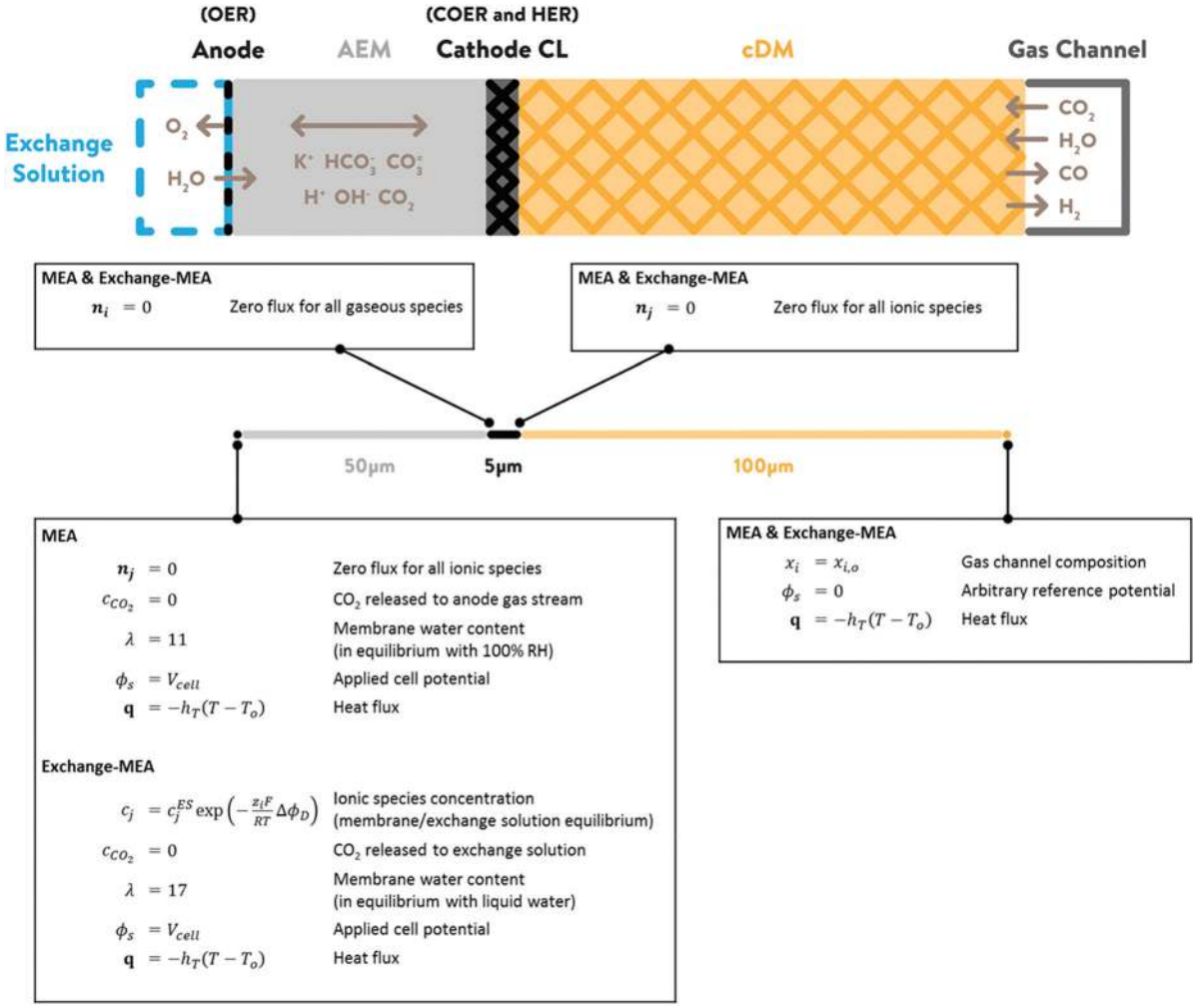

Fig. 1 Schematic of modeling framework and boundary conditions.

as the proton source for the reaction.[28] For this reason, the alkaline reaction is used for COER,

$$CO_2 + H_2O + 2e^- \rightarrow CO + 2OH^- \quad (5)$$

The ionomer membrane electrolyte has a fixed positive charge concentration, c_M, determined by the product of its ion-exchange capacity, IEC, and its density, ρ_M. We use properties of a Tokuyama A201 membrane, listed in Table 1. The water content, λ, describes the extent of hydration of the membrane, and is defined as the number of water molecules per cationic group in the membrane. For simplicity, we use the water-uptake isotherm measured by Peng *et al.* for a HCO_3^- AEM at 25 °C, and ignore its dependence on the anion type and temperature.[29] Water-uptake isotherms reported for several Tokuyama A201 membranes show a weak dependence on temperature.[29–31] Results of temperature-dependent membrane isotherms are discussed in the ESI.† Additionally, the membrane is determined to be primarily in the $HCO_3^-/CO_3^=$ form (discussed later), making the HCO_3^- form of the isotherm a reasonable approximation. The water-uptake isotherm also describes the relationship between water concentration and water activity in the membrane.

Homogeneous reactions, including bicarbonate buffer and water-dissociation reactions, occur in the ionomer and aqueous phases,

$$CO_2(aq) + H_2O \xleftrightarrow{k_1,k_{-1}} H^+ + HCO_3^- \quad K_1 \quad (6)$$

$$HCO_3^- \xleftrightarrow{k_2,k_{-2}} H^+ + CO_3^{2-} \quad K_2 \quad (7)$$

$$CO_2(aq) + OH^- \xleftrightarrow{k_3,k_{-3}} HCO_3^- \quad K_3 \quad (8)$$

$$HCO_3^- + OH^- \xleftrightarrow{k_4,k_{-4}} H_2O + CO_3^{2-} \quad K_4 \quad (9)$$

$$H_2O \xleftrightarrow{k_w,k_{-w}} H^+ + OH^- \quad K_w \quad (10)$$

Here, K_n denotes the equilibrium constant for reaction n, calculated from van't Hoff equation using the change of entropy, ΔS_n, and the heat of reaction, ΔH_n, listed in Table 1

$$K_n = \exp\left(\frac{\Delta S_n}{R}\right)\exp\left(-\frac{\Delta H_n}{RT}\right) \quad (11)$$

The kinetics of these reactions are described using the rate coefficients measured by Shultz *et al.* rounded to the nearest

Table 1 List of parameters

Parameter	Value	Unit	Ref.
Membrane			
L_M	5×10^{-5}	M	
IEC	1.7	mmol g^{-1}	29
ρ_M	1.2	g ml^{-1}	29
DM			
L_{DM}	10^{-4}	M	
ε_{DM}	0.8		
$r_{p,DM}$	7.33×10^{-7}	M	38
σ_{DM}	220	S m^{-1}	39
$\kappa^{o}_{sat,DM}$	1.72×10^{-11}	m^2	40
$k_{T,DM}$	0.015	W m^{-1} K^{-1}	41
CL			
L_{CL}	5×10^{-6}	M	
ε_{CL}	0.5		
$r_{p,CL}$	25×10^{-7}	M	38
a_v	10^7	m^{-1}	42
σ_{CL}	100	S m^{-1}	39
$\kappa^{o}_{sat,CL}$	8×10^{-16}	m^2	40
$k_{T,CL}$	0.003	W m^{-1} K^{-1}	41
Gas species properties			
ν_{p,H_2}	7.07		43
ν_{p,H_2O}	12.7		43
$\nu_{p,CO}$	18.9		43
ν_{p,CO_2}	26.9		43
p_{vap}	$10^{8.07-\frac{1730.63}{T\,[K]-39.724}}$	mmHg	44
H_{CO_2}	$34\exp\left(2400\left(\frac{1}{T\,[K]}-\frac{1}{298}\right)\right)$	mM atm^{-1}	44
Aqueous species properties			
D_{K^+}	$1.96 \times 10^{-5}\exp\left(-2300\left(\frac{1}{T\,[K]}+\frac{1}{298}\right)\right)$	cm^2 s^{-1}	45
D_{H^+}	$4.49 \times 10^{-5}\exp\left(-1430\left(\frac{1}{T\,[K]}+\frac{1}{273}\right)\right)$	cm^2 s^{-1}	46
D_{OH^-}	$2.89 \times 10^{-5}\exp\left(-1750\left(\frac{1}{T\,[K]}+\frac{1}{273}\right)\right)$	cm^2 s^{-1}	46
$D_{HCO_3^-}$	$7.016 \times 10^{-5}\left(\frac{T\,[K]}{204.03}-1\right)^{2.3942}$	cm^2 s^{-1}	47
$D_{CO_3^-}$	$5.447 \times 10^{-5}\left(\frac{T\,[K]}{210.26}-1\right)^{2.1919}$	cm^2 s^{-1}	47
D_{CO_2}	$2.17 \times 10^{-5}\exp\left(-2345\left(\frac{1}{T\,[K]}+\frac{1}{303}\right)\right)$	cm^2 s^{-1}	44
D_w	$9 \times 10^{-17}\exp(5.9a_w)$	cm^2 s^{-1}	29
Homogeneous reactions			
S_1	−96.31	J mol^{-1} K^{-1}	44
S_2	−148.1	J mol^{-1} K^{-1}	44
S_w	−80.66	J mol^{-1} K^{-1}	44
H_1	7.64	kJ mol^{-1}	44
H_2	14.85	kJ mol^{-1}	44
H_w	55.84	kJ mol^{-1}	44
k_1	10^{-2}	s^{-1}	32
k_2	10^2	s^{-1}	32
k_3	10^3	L mol^{-1} s^{-1}	32
k_4	10^9	L mol^{-1} s^{-1}	32
k_w	10^{-3}	mol L^{-1} s^{-1}	32
Charge transfer reactions			
Π_{OER}	$240\frac{T\,[K]}{298}$	mV	41
Π_{HER}	$13\frac{T\,[K]}{298}$	mV	Approximated

Table 1 (*continued*)

Parameter	Value	Unit	Ref.
Π_{COER}	$40\frac{T\ [K]}{298}$	mV	Approximated
Others			
$h_{T,liquid}$	10^4	W m^{-2} K^{-1}	Assumed
$h_{T,gas}$	10^3	W m^{-2} K^{-1}	Assumed

order of magnitude.[32] Results by Divekar *et al.* suggest that these rate coefficients, as well as equilibrium constants, likely differ in an ionomer compared to those for an aqueous solution;[33] however, to the best of our knowledge, the magnitudes of these differences have not been established, and are likely to vary with membrane hydration, counterion identity, *etc.*[34,35] Such investigation is beyond the scope of the current efforts. The effects of varying the rate of reaction for eqn (8) are discussed in the ESI† (Fig. S2).

The CL and DM are both porous structures. The solid fraction of the CL is composed of Ag nanoparticles in an ionomer binder, and the DM is a hydrophobic carbon-fiber structure. We assume that the thickness of the anionic ionomer coating the Ag nanoparticles within the CL is 10 nm, which is sufficient to provide an ionic pathway for anions between the catalyst nanoparticles and the membrane.[36] The DM is assumed to remain liquid free, which is reasonable considering its hydrophobic nature and existence of a temperature gradient discussed later.

The MEA model is built upon framework of the GDE model we reported previously.[37] The governing equations and a list of parameters are summarized in Tables 2–4. The model describes five main physical phenomena: transport of neutral and ionic species (including diffusion, migration, and convection), fluid flow through a porous medium, current and (over)potential distribution, chemical (homogeneous) and electrochemical (heterogeneous) reactions, and heat transfer. The model applies conservation of mass, momentum, charge, and energy to solve for the following state variables: mole fractions of gaseous species CO_2, H_2O, CO, and H_2 in the cathode GDE, concentrations of dissolved CO_2 and H_2O in the membrane and ionomer, concentrations of ionic species K^+, H^+, OH^-, HCO_3^-, $CO_3^{=}$ in the membrane and ionomer, gas-phase velocity in the cathode GDE, potentials of the solid-phase electrode and ionic-phase electrolyte, and temperature of the MEA. Fig. 1 provides an overview of the boundary conditions imposed. Below, we discuss in further detail relevant equations used to obtain effective parameter values, the source terms in each phase, and the boundary conditions for the three cases studied in this paper: full-MEA, 0.5 M $KHCO_3$ exchange-MEA, and 0.5 M KOH exchange-MEA.

Table 2 Governing equations (see nomenclature for symbol definitions)

Solid phase variable: ϕ_s	
$\nabla\cdot\mathbf{i}_s = -\nabla\cdot\mathbf{i}_l = -a_v\sum_k \mathbf{i}_k$	(12)
$\mathbf{i}_s = -\sigma_s^{eff}\nabla\phi_s$	(13)
Aqueous phase variables: $\omega_j, j = CO_2(l), K^+, H^+, OH^-, HCO_3^-, CO_3^{=}, H_2O$; ϕ_l	
$\nabla\cdot\mathbf{n}_j = R_{CT,j} + R_{B,j} + R_{PT,j}$	(14)
$\mathbf{n}_{j\neq H_2O} = -D_j^{eff}\rho_l\nabla\omega_j + \frac{z_jF}{RT}D_j^{eff}\rho_l\omega_j\nabla\phi_l$	(15)
$\mathbf{n}_w = -D_w\rho_l\nabla\omega_w + \sum_j\frac{\xi_j\mathbf{n}_j}{M_j}$	(16)
$\sum_j\frac{z_j\omega_j}{M_j} = 0$	(17)
Gas phase variables: ω_i, $i = CO_2(g), CO, H_2, H_2O$; p_G	
$\nabla\cdot\mathbf{n}_i = R_{CT,i} + R_{B,i} + R_{PT,i}$	(18)
$\mathbf{n}_i = \mathbf{j}_i + \rho_i\mathbf{u}_g$	(19)
$\mathbf{j}_i = -\rho_g D_i^{eff}\nabla\omega_i - \rho_g D_i^{eff}\omega_i\frac{\nabla M_n}{M_n}$	(20)
$\mathbf{u}_g = -\frac{\kappa_m^{eff}}{\mu_g}\nabla p_G$	(21)
$\sum_i\omega_i = 1$	(22)
Energy variable: T	
$\nabla\cdot\mathbf{q} = Q_{CT} + Q_B + Q_J$	(23)
$\mathbf{q} = -k_{T,m}\nabla\mathbf{T}$	(24)

Table 3 Model parameter equations (see nomenclature for symbol definitions)

$D_j^{eff} = \varepsilon_L^q\frac{D_{i,w}}{x_w(1+\zeta_i)}$	(25)
$D_i^{eff} = \frac{\varepsilon_m}{\tau_m}D_i = \varepsilon_m{}^{3/2}\left(\frac{1}{D_i^{SM}} + \frac{1}{D_i^{K}}\right)^{-1}$	(26)
$D_i^{SM} = \frac{1-\omega_i}{\sum_{n\neq i}\frac{y_n}{D_{in}}}$	(27)
$D_i^{K} = \frac{2r_{p,m}}{3}\sqrt{\frac{8RT}{\pi M_i}}$	(28)
$D_{iq}\ [cm^2\ s^{-1}] = \frac{10^{-3}T\ [K]^{1.75}\left(M_i\ [g\ mol^{-1}]^{-1} + M_q\ [gmol^{-1}]^{-1}\right)^{0.5}}{p\ [atm]\left(v_{p,i}{}^{0.33} + v_{p,q}{}^{0.33}\right)^2}$	(29)

Electrolyte/ionomer membrane equilibrium

The fixed background charge of an ionomer membrane leads to an electric potential difference at the membrane (ϕ_l^M)/exchange solution (ϕ_l^E) interface, the Donnan potential: $\Delta\phi_D = \phi_l^M - \phi_l^E$. At equilibrium, the electrochemical potential of each species in the two phases must be equal, resulting in the following

Table 4 Source terms (see nomenclature for symbol definitions)

$$R_{\mathrm{CT},i} = -M_i \sum_k \frac{s_{i,k} a_\mathrm{v} \mathbf{i}_k}{n_k F} \tag{30}$$

$$R_{\mathrm{B},j} = M_j \sum_n s_{j,n} \left(k_n \prod_{s_{j,n}<0} c_j^{-s_{j,n}} - \frac{k_n}{K_n} \prod_{s_{j,n}>0} c_j^{s_{j,n}} \right) \tag{31}$$

$$R_{\mathrm{PT},j} = -R_{\mathrm{PT},i} = a_\mathrm{v} M_j \frac{D_j^{\mathrm{eff}}}{\delta_{\mathrm{TF}}} \left(c_j^{\mathrm{g}} - c_j \right) \tag{32}$$

Species	R_{CT}	R_{B}	R_{PT}
CO_2(g)	—	—	Gas/ionomer
H_2O(g)	—	—	Gas/ionomer
CO(g)	COER	—	—
H_2(g)	HER	—	—
CO_2(l)	COER	Eqn (6) and (8)	Gas/ionomer
H_2O(l)	OER, HER, COER	Eqn (6), (9) and (10)	Gas/ionomer
K^+	—	—	—
H^+	OER, HER	Eqn (6), (7) and (10)	—
OH^-	OER, HER, COER	Eqn (8)–(10)	—
HCO_3^-	—	Eqn (6)–(9)	—
$CO_3^=$	—	Eqn (7) and (9)	—

relationship between species concentration in the membrane, c_i^{M}, and in the exchange solution, c_i^{E},

$$c_i^{\mathrm{M}} = c_i^{\mathrm{E}} \exp\left(-\frac{z_i F}{RT} \Delta\phi_{\mathrm{D}} \right) \tag{33}$$

The Donnan potential can then be determined by enforcing electroneutrality in the membrane, taking into consideration the background charge. $\Delta\phi_{\mathrm{D}}$ is positive for an AEM, due to its fixed positive background charge. This creates an extra energy barrier for cations to enter the membrane ($z_i > 0$, so the exponential term is less than unity), but does not necessarily completely exclude cations from the membrane. For simplicity, species concentration and the ionic potential in the membrane will be denoted as c_i and ϕ_{l}, respectively, for the remainder of the paper.

Electron transport and charge transfer reactions

The solid-phase electronic potential, ϕ_{s}, is described by charge conservation, eqn (12), and Ohm's law, eqn (13). Charge-transfer reactions occur at the electrode/electrolyte interface, and can be described by the Tafel equation for overpotentials greater than 0.2 V (with less than 0.01% error compared to Butler–Volmer equation),[48]

$$\mathbf{i}_k = -i_{\mathrm{o},k} \left(\frac{c_j}{c_j^{\mathrm{ref}}} \right)^{\gamma_k} \exp\left(-\frac{\alpha_{\mathrm{c},k} F}{RT} \eta_k \right) \tag{34}$$

Here, γ_k is the reaction order with respect to some reactant, $\alpha_{\mathrm{c},k}$ is the cathodic transfer coefficient, and η_k is the overpotential for reaction k. The exchange current density, $i_{\mathrm{o},k}$, depends on the pre-exponential factor, A_k, and the apparent activation energy, $E_{\mathrm{a},k}$, according to the Arrhenius equation,

$$i_{\mathrm{o},k} = A_k \exp\left(-\frac{E_{\mathrm{a},k}}{RT} \right) \tag{35}$$

Studies have shown that the activation energy for the HER is pH-dependent, with a slope of approximately 1 (kJ mol^{-1})/pH.[49–55] For the OER, we also assumed a linear dependence of E_{a} on pH and obtained a slope of, coincidentally, 1 (kJ mol^{-1})/pH from a fit to the experimental data reported by Kuo *et al.*[56] Designing electrocatalysts that lower the energy barrier for CO_2R products and improve CO_2R activity is an area of active research; the effects of $i_{\mathrm{o,COER}}$ on MEA performance are described in the ESI.† We note that such rate expressions are used empirically to capture the pH-dependence observed in experiments. The pre-exponential factors were fit to the exchange current densities reported in the references listed in Table 5; all kinetic parameters, including the standard electrode potential relative to the standard hydrogen electrode (SHE) of reaction k, U_k^{o}, are summarized in Table 5.

Charge-transfer reactions contribute to source terms, $R_{\mathrm{CT},i}$, as listed in eqn (30); they apply to aqueous species CO_2, OH^-, and H^+, and for gaseous species CO and H_2. The electronic potential is set to $\phi_{\mathrm{s}} = 0$ at the cathode boundary, and varied from 2 to 4 V (cell voltage) at the anode boundary.

Ionic and neutral species transport and acid/base reactions in the ionomer

Mass conservation, eqn (14), and the Nernst–Planck equation, eqn (15), govern the transport of ionic and neutral species and the electrolyte potential profile, ϕ_{l}, in the ionomer. Commonly, Stefan–Maxwell diffusion is used to capture species/species interaction that become significant under non-dilute conditions. However, using the Stefan–Maxwell approach would introduce 28 additional degrees of freedom, and require that composition-dependent diffusion coefficients be determined (frictional interactions between six species, water, and membrane). Since this would considerably increase the uncertainty and the complexity of our numerical model, we resort to using Nernst–Planck equation for our system even though we are not necessarily under dilute conditions. For water, electro-osmosis replaces

Table 5 Kinetic parameters for charge transfer reactions

	U_k^{o} (V)	A_k (mA cm^{-2})	E_{a} (kJ mol^{-1})	$\alpha_{\mathrm{a/c}}$	$\left(\frac{c_i}{c_i^{\mathrm{ref}}}\right)^{\gamma_i}$	Ref.
Anode						
OER acid	1.23	9.40×10^{-7}	11 + 1 × pH	1.5	—	56–58
OER base		1.23×10^{-4}			$[OH^-]/(1\ \mathrm{M})$	
Cathode						
HER acid	0	2.77×10^{19}	83 + 1 × pH	0.44	$[H^+]/(1\ \mathrm{M})$	49–55
HER base		8.84×10^{6}			—	
COER	−0.11	7.25×10^{8}	100	1	$([CO_2]/(1\ \mathrm{M}))^{1.5}$	26, 27 and 59

migration, represented by the second term on the right side of eqn (16), and thus some of the coupling between frictional forces is maintained. The electro-osmotic coefficients for water carried by ionic species i (ξ_i) have not been well characterized for AEMs in the presence of CO_2. Therefore, we adopt a value of one for the electro-osmotic coefficients, consistent with what is commonly used for a vapor-equilibrated CEM and close to the experimentally measured 0.61 ± 0.12 for a vapor-equilibrated, OH^- form of the Tokuyama A201 membrane.[60,61] The electro-osmotic coefficient tends to be higher for a liquid-equilibrated membrane, and has been reported to range from 2 to 7 for a KOH-equilibrated AEM.[30,62] We note that our model proved not to be strongly dependent on the value of the electro-osmotic coefficient (see Fig. S3, ESI†), so a value of one was used for all scenarios.

The effective diffusion coefficient for species other than H_2O in the membrane, $D_{j,\mathrm{M}}^{\mathrm{eff}}$, is calculated using eqn (25) in Table 3 following Grew *et al.*[63,64] The water mole fraction, x_w, and water volume fraction in the ionomer, ε_L, are defined as

$$x_\mathrm{w} = \frac{\lambda}{1+\lambda} \tag{36}$$

and

$$\varepsilon_\mathrm{L} = \frac{\lambda V_\mathrm{w}}{\lambda V_\mathrm{w} + V_\mathrm{M}} \tag{37}$$

respectively, where $V_\mathrm{M} = 1/(\mathrm{IEC}\cdot\rho_\mathrm{M})$ and V_w are the molar volume of the membrane and water, respectively. ζ_i describes the ratio of species-water and species-membrane interaction and is approximated from kinetic theory to be[65]

$$\zeta_i = \frac{1}{\lambda}\left(\frac{V_\mathrm{M}}{V_\mathrm{w}}\right)^{2/3}\left(\frac{M_{i,\mathrm{M}}}{M_{i,\mathrm{w}}}\right)^{1/2} \tag{38}$$

where $M_{i,\mathrm{M}} = \left(\frac{1}{M_i} + \frac{1}{M_\mathrm{M}}\right)^{-1}$ is the reduced molar mass. Water diffusivity in the membrane, $D_{\mathrm{w,M}}$, is a function of ionomer water activity, a_w, as measured by Peng *et al.*, and fit to the expression listed in Table 1.[29] Finally, source terms due to homogeneous bulk reactions, $R_{\mathrm{B},j}$, eqn (31) in Table 4, are calculated using apparent rate coefficients (Table 1), which were approximated based on values reported by Schulz *et al.* rounded to the nearest order of magnitude.[32] Water activity instead of water concentration is used for homogeneous reactions involving water to ensure that equilibrium can be established at the electrolyte/ionomer membrane interface. $R_{\mathrm{B},j}$ applies to aqueous species involved in reactions listed in eqn (6)–(10). Other source terms for aqueous species include charge-transfer reactions, eqn (30), discussed in the previous section, and phase-transfer reactions, eqn (32), discussed in the following section.

The flux for all species is set to zero at the CL/DM boundary at the cathode. At the anode boundary, CO_2 and H_2O are taken to be in equilibrium with the anode feed gas (inert gas N_2 with 100% RH). The flux for all ionic species is set to zero for the full-MEA case, and for the exchange-MEA cases, all species are taken to be in equilibrium with the exchange solution, which is assumed to be at constant concentration. The anode boundary condition assumes fresh exchange solution being circulated at a high flowrate in the anode channel.

Gas-phase species transport

Concentration profiles for gaseous species are determined within the CL and DM domains. The Stefan–Maxwell equation, eqn (20) and Darcy's law, eqn (21) are used to describe the diffusion and convection terms, respectively. The effective diffusivity is an average of the Stefan–Maxwell diffusivity, D_i^{SM}, and Knudsen diffusivity, D_i^{K} (assuming both forms of diffusion occur in parallel) and is corrected for the porosity, ε_m, and the tortuosity, τ_m, of medium m using Bruggeman's relationship, eqn (26)–(28). The binary gas-phase diffusion coefficients are calculated using the equation derived by Fuller *et al.*, eqn (29), where $v_{\mathrm{p},i}$ is the diffusion volume of species i, listed in Table 1.[43]

The source terms for gaseous species occur in the CL domain. They include the charge transfer reactions producing H_2 and CO, eqn (30), and the adsorption/desorption of CO_2 and H_2O into/out of the ionomer, $R_{\mathrm{PT},i}$, eqn (32). The volumetric rate of gas dissolution into the ionomer phase is estimated using Fick's law, where c_j^g is the concentration of species i in equilibrium with its gas-phase concentration. For H_2O, $c_\mathrm{w}^\mathrm{g} = c_\mathrm{M}\lambda^g$, where λ^g corresponds to the water content in equilibrium with water activity $a_\mathrm{w} = p_\mathrm{G}y_\mathrm{w}/p_\mathrm{vap}$, obtained using the isotherm reported by Peng *et al.*;[29] for CO_2, $c_{\mathrm{CO_2}}^\mathrm{g} = H_{\mathrm{CO_2}}p_\mathrm{G}y_{\mathrm{CO_2}}$ where $H_{\mathrm{CO_2}}$ is the temperature-dependent Henry's constant for CO_2, listed in Table 1. It should be noted that the ionomer and salinity effects of the water vapor pressure are not accounted for, since these are estimated to be small. H_2 and CO are neglected in the ionomer phase based on their limited solubility in water, an order of magnitude lower than CO_2.[44] The fluxes of all gaseous species are set to zero at the membrane/CL boundary, and their mass fractions set to the cathode feed gas composition at the GDL/gas channel boundary.

Energy transport

There are three sources of heat generation in the system: heat generated from charge-transfer reactions at the two electrodes, Q_CT, the heat of reaction from homogeneous bulk bicarbonate buffer reactions, Q_B, and Joule heating, Q_J. Q_CT consists of both irreversible losses and reversible heat generation,[48]

$$Q_\mathrm{CT} = \sum_k \left(i_k\eta_k + i_k\Pi_k\right) \tag{39}$$

where Π_k is the Peltier coefficient for reaction k, listed in Table 1. Π_COER was approximated from the change in entropy for the overall reaction $2CO_2 \Leftrightarrow 2CO + O_2$.[41,48]

$$\frac{\Pi_\mathrm{COER}}{T} = \frac{\Delta S}{nF} - \frac{\Pi_\mathrm{OER}}{T} \tag{40}$$

The term Q_B results from the change in enthalpy, ΔH_n, for homogeneous reactions listed in eqn (6)–(10),

$$Q_\mathrm{B} = \sum_n \Delta H_n\left(k_n\prod_{s_{j,n}<0} c_j^{-s_{j,n}} - \frac{k_n}{K_n}\prod_{s_{j,n}>0} c_j^{s_{j,n}}\right) \tag{41}$$

Finally, Joule heating due to electrical resistance is determined by,

$$Q_J = \frac{i_s^2}{\sigma_m} \quad (42a)$$

or

$$Q_J = \frac{i_l^2}{\kappa_l} \quad (42b)$$

for the solid and ionomer phase, respectively. The ionomer-phase conductivity is derived from the Nernst–Planck equation,[48]

$$\kappa_l = \frac{F^2}{RT}\sum_j z_j^2 c_j D_j^{eff} \quad (43)$$

A Robin boundary condition is set at the two boundaries using a heat transfer coefficient, h_T, to describe the heat flux, driven by the difference between the cell temperature at that boundary and room temperature, T_0.

$$q_T = -h_T(T - T_0) \quad (44)$$

Numerical method

The governing equations are solved using the MUMPS general solver in COMSOL Multiphysics 5.3a with a relative tolerance of 0.001. The modelling domain has a maximum element size of 0.01 μm. Element sizes were decreased to 0.001 μm near the boundaries to capture sharp concentration gradients. The base-case model has been provided in the ESI.†

Results and discussion

Dependence of the ohmic drop on cell configuration

An order-of-magnitude improvement in the CO_2R current density occurs in moving from a planar cathode to a GDE cathode configuration due to the increased active surface area and decreased mass-transfer resistances associated with the latter configuration.[37] Simply substituting the planar cathode with a GDE cathode (aqueous GDE cell shown in Fig. 2) results in an order-of-magnitude increase in the ohmic drop when the total current density is increased from 10 to 100 mA cm^{-2}, rendering such cell designs impractical for industrial application. By

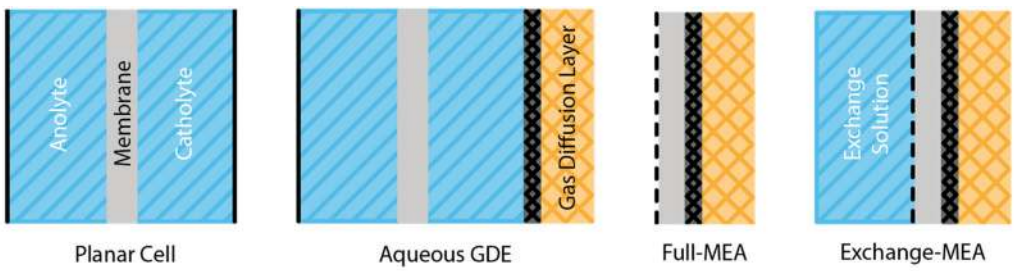

Potential distribution	Planar (10 mA cm^{-2})	Aqueous GDE (100 mA cm^{-2})	Full-MEA & Exchange-MEA (100 mA cm^{-2})
Thermodynamic potential under normal conditions (V) (OER + COER)	1.34		
Cathode overpotential (V)	1.1[59]	0.7[37]	0.7[37]
Anode overpotential (V)	0.3*	0.4*	0.4*
Electrolyte ohmic potential (V) (0.5 M $KHCO_3$, 6 S m^{-1})	0.2**	2**	0
Membrane ohmic potential (V) (50 μm, 0.5 S m^{-1})	0.01	0.1	0.1
Total cell potential (V)	**2.95**	**4.54**	**2.54**

**assuming OER on planar IrO_2, approximated from Butler-Volmer equation fitted to experimental data[66]*
***assuming 1 cm distance between anode and cathode*

Fig. 2 Graphical illustration for various cell designs and a breakdown of the applied voltage. There is a 44% reduction in applied voltage for MEA compared to the aqueous GDE cell at the same total current density.

comparison, both the full-MEA and exchange-MEA eliminate the large ohmic drop by removing the electrolyte compartments and significantly decreasing the anode–cathode distance, allowing the cell to maintain the 100 mA cm^{-2} current density with a 44% reduction in the applied cell voltage. The values in Fig. 2 are first-order approximations and do not include effects such as concentration polarization, temperature changes, membrane dehydration, *etc.*; additional details on the approximation method are included in the ESI.† A mesh-like structure or GDE is required for the anode in the full-MEA and exchange-MEA designs where OER occurs to prevent layer delamination caused by the evolution of oxygen bubbles.

While the full-MEA and exchange-MEA minimize the ohmic loss across the cell, reactant and product crossover becomes a concern due to the small distance between the two electrodes. For an Ag cathode, almost no liquid product is produced and the CO solubility is low, limiting the CO crossover current density to approximately 1 mA cm^{-2} at room temperature (estimated using Fick's law and the solubility and diffusivity of CO in water). It should be noted though that the aqueous GDE cells can serve diagnostic purposes due to their isolation of a single electrode and easier implementations of a reference electrode for interrogation possibilities.[13] The GDE type designs though are efficiency and performance cells due to the reasons above.

Applied voltage breakdown and precipitation issues for a full-MEA and exchange-MEAs

Fig. 3 shows the (a) total current density (TCD) and (b) CO FE for the three cases considered: full-MEA, 0.5 M $KHCO_3$ exchange-MEA, and 0.5 M KOH exchange-MEA. The exchange-MEA's produce a higher TCD and CO FE than the full-MEA at the same applied cell potential, with the KOH exchange-MEA achieving the highest performance. The variance in CO FE for the three cases can be explained by the cathode pH: the alkalinity at the cathode increases in the order MEA < $KHCO_3$ exchange-MEA < KOH exchange-MEA because of the exchange solution, as well as the higher TCD producing OH^- at a higher rate at the cathode.

To understand the trend observed for the TCD, we plot the applied voltage breakdown (AVB) for the three cases (Fig. 3c, e and f). The applied voltage is comprised of the thermodynamic potential, the kinetic overpotential, and the transport overpotential (Nernstian plus ohmic components). The thermodynamic potential depends on the species concentrations near the two electrodes at the open circuit. Assuming that all gaseous species are at normal conditions, the thermodynamic potential, η_{th}, for a cell performing OER at the anode and COER at the cathode can be calculated as

$$\eta_{th} = \left(U^{o}_{OER} - U^{o}_{COER}\right) + \frac{RT}{F}\ln\left(\frac{c^{C}_{OH^-}}{c^{A}_{OH^-}}\right) \quad (45)$$

where $c^{C}_{OH^-}$ and $c^{A}_{OH^-}$ refers to the OH^- concentration at the cathode and anode, respectively. The Nernstian overpotential is defined as the potential developed due to the change in OH^- concentration at the electrode relative to that at open circuit,

$$\eta_N = \pm\frac{RT}{F}\ln\left(\frac{c_{OH^-}}{c^{o}_{OH^-}}\right) \quad (46)$$

The sign on the right side is negative for the anode and positive for the cathode. Therefore, a higher OH^- concentration at the anode during operation would result in a negative (more favorable) Nernstian overpotential, while a higher OH^- concentration at the cathode leads to a positive (less favorable) Nernstian overpotential. The applied voltage is broken down for OER and COER, since CO is the product of interest, and the CO FE reaches almost 100% for all cases above a cell potential of 2.5 V. The voltage contributions to the OER and HER can be calculated analogously.

Comparing the AVB for the three cases, it is clear that the exchange-MEAs substantially minimize two overpotential sources observed in the full-MEA case: the anode Nernstian potential and the ohmic drop. The anode Nernstian potential is eliminated in the exchange-MEAs because the local environment at the anode is maintained by the circulating exchange solution. In contrast, sharp concentration gradients develop in the full-MEA and increase with increasing TCD, as shown in Fig. 4a. The exchange solution also improves membrane hydration, and, consequently, its conductivity, thereby decreasing the ohmic drop across the cell. For a full-MEA, the membrane water content decreases with increasing current density (Fig. 5a) because the water concentration in the gas channel is limited to its vapor pressure and water is transported and consumed in the reactions. Furthermore, as the temperature of the cell increases (Fig. 5d), the gas-phase RH decreases (Fig. 5b) even though the partial pressure of water increases (Fig. 5c), causing water in the CL ionomer to evaporate. Finally, the KOH exchange solution reduces the thermodynamic potential of the system due to the OH^- concentration gradient that develops: the anode remains at the concentration of the circulating KOH solution, while the OH^- concentration is lower near the cathode as the CO_2 feed at the cathode gas channel neutralizes the OH^- (Fig. 4b). The concentration profile where the anode OH^- concentration is higher than that at the cathode is opposite to the one established for the full-MEA and $KHCO_3$ exchange-MEA, resulting in a lower thermodynamic potential, or a negative (more favorable) Nernstian potential. A higher OH^- concentration at the anode compared to the cathode makes the second term on the right side of eqn (45) negative, thereby decreasing the thermodynamic overpotential for the KOH exchange-MEA (Fig. 3f).

The main limitation for the exchange-MEAs is the precipitation of K_2CO_3 at the cathode. Driven by both the chemical and electric potential gradients, K^+ exchanges with H^+ produced at the anode and moves to the cathode. Eventually, at ~750 mA cm^{-2}, the concentration of K_2CO_3 exceeds its solubility limit and it precipitates at the cathode (indicated by the red crosses in Fig. 3a). Therefore, batch operation with salt removal is required to operate exchange-MEAs at current densities above that where precipitation can occur. It is possible to offset this precipitation limit by

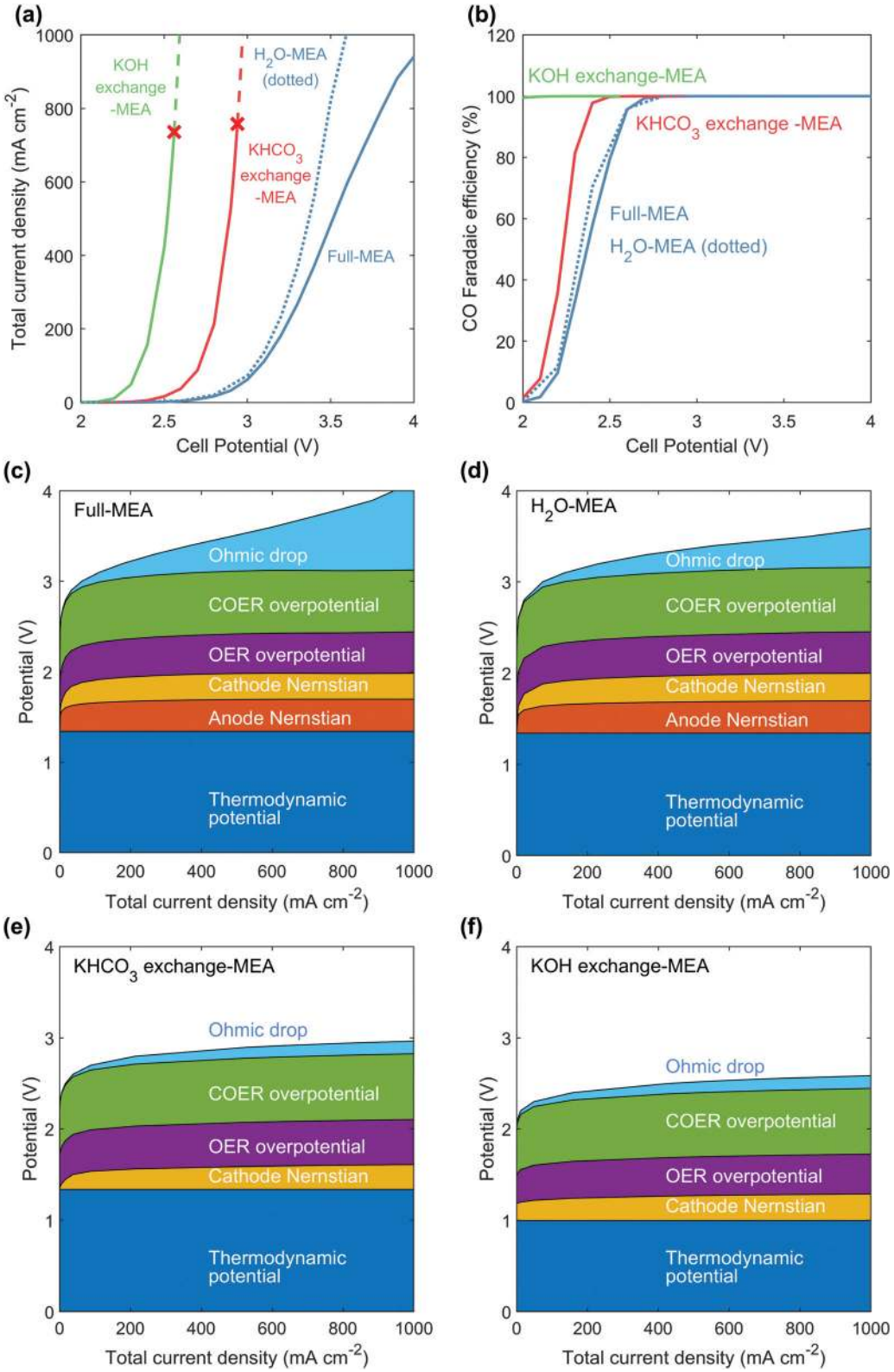

Fig. 3 (a) The total current density and (b) the CO faradaic efficiency (FE) for the four cases considered and their applied voltage breakdown (AVB), (c) full-MEA, (d) H_2O-MEA, (e) $KHCO_3$ exchange-MEA, and (f) KOH exchange-MEA. Dashed line in (a) represent current densities at which salt precipitations and batch operation is required. Cathode feed composition is 97 mol% CO_2 and 3 mol% H_2O.

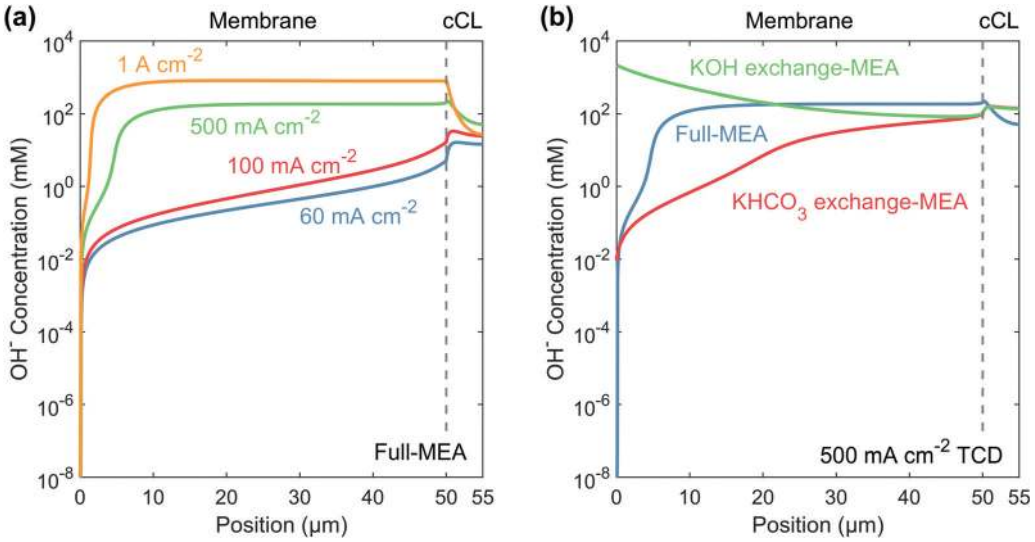

Fig. 4 Hydroxide concentration across (a) a full-MEA at 60, 100, 500 and 1000 mA cm^{-2}; and (b) at 500 mA cm^{-2} comparing full-MEA, $KHCO_3$ exchange-MEA, and KOH exchange-MEA. The hydroxide concentration across the full-MEA increases with increasing current density, creating significant concentration (Nernstian) overpotentials. In the case of KOH exchange-MEA, the hydroxide concentration is reversed due to the bicarbonate buffer reactions at the cathode side, resulting in a negative Nernstian overpotential.

feeding liquid water to the anode in order to provide better hydration. A H_2O-MEA improves the total current density (but not the CO FE) of the full-MEA due to better membrane hydration, but does not provide the same advantageous as an exchange-MEA with dissolved salt (Fig. 3d) because of its inability to exchange ions. Thus, exchange-MEAs exhibit low voltage for a given current density but the full-MEA allows achievement of higher current densities without consideration of additional engineering controls.

Ion transport and the charge-carrying species in a full-MEA

At equilibrium, an OH^- form AEM exposed to CO_2 will convert to $HCO_3^-/CO_3^=$ form due to bicarbonate buffer reactions (6)–(9). The ratio of $HCO_3^-/CO_3^=$ depends on the partial pressure of CO_2 in contact with the membrane and has been measured experimentally for an AEM exposed to 400 ppm CO_2.[33,67] Fig. 6 shows the distribution of anion fraction ($|z_i c_i|/c_M$) across the MEA for low, medium, and high current densities. As the current density increases, the membrane gradually converts to the $CO_3^=$ form, and eventually to the OH^- form starting from the cathode side. This occurs because OH^- is produced by the COER and HER (see eqn (4) and (5)) at the cathode. OH^- reacts with the HCO_3^- initially in the membrane to form $CO_3^=$; OH^- also reacts with dissolved CO_2 to form HCO_3^- and eventually $CO_3^=$. The $CO_3^=$ then transports from the cathode to the anode, driven by its concentration gradient (diffusion), and the potential gradient (migration). At the anode, bicarbonate buffer reactions drive the conversion of $CO_3^=$ to HCO_3^- and eventually back to CO_2, which is released into the anode gas channel. As the current density increases, the rate of OH^- production at the cathode also rises, eventually exceeding the homogeneous reaction rates, resulting in accumulation of OH^- at 500 mA cm^{-2} and 1 A cm^{-2}, as shown in Fig. 6c and d.

Regarding the transport and distribution of species across the MEA: (1) $CO_3^=$ is the main charge carrying species for a full-MEA with an AEM performing CO_2R, consistent with experimental observations reported by Liu *et al.*[68] The HCO_3^- diffusion flux from anode to cathode is larger than its migration flux from cathode to anode, which means HCO_3^- is moving against the flow of current. OH^- begins to accumulate at high current densities and the membrane will eventually return to the OH^- form as the charge-transfer rate exceeds the homogeneous reaction rates. (2) A portion of the CO_2 fed at the cathode is transported as $CO_3^=$ and eventually released as CO_2 at the anode for a full-MEA. CO_2 in the anode gas outlet has also been observed by Liu *et al.* and Pătru *et al.*[68,69] For $KHCO_3$ exchange-MEA and KOH exchange-MEA, CO_2 can be flushed out as $HCO_3^-/CO_3^=$ by the exchange solution. While helpful in terms of performance, this becomes a source of inefficiency for the system as discussed below.

CO_2 utilization efficiency and observed limitations

The CO_2 losses need to be defined and quantified as a function of operating conditions because a portion of the CO_2 is consumed homogeneously at the cathode, transported to and released at the anode (*i.e.*, electrochemically pumped in a similar fashion as that observed in AEM fuel cells[70]), as expected from reactions (6)–(10) and the transport equations in Table 2. Using the gaseous species fluxes obtained from the model and assuming a 50 sccm CO_2 feed at 100% RH (97 mol% CO_2), the CO_2 consumption (the percentage of CO_2 feed that is consumed either electrochemically or by homogeneous reactions) and the CO_2 conversion (the percentage of CO_2 feed

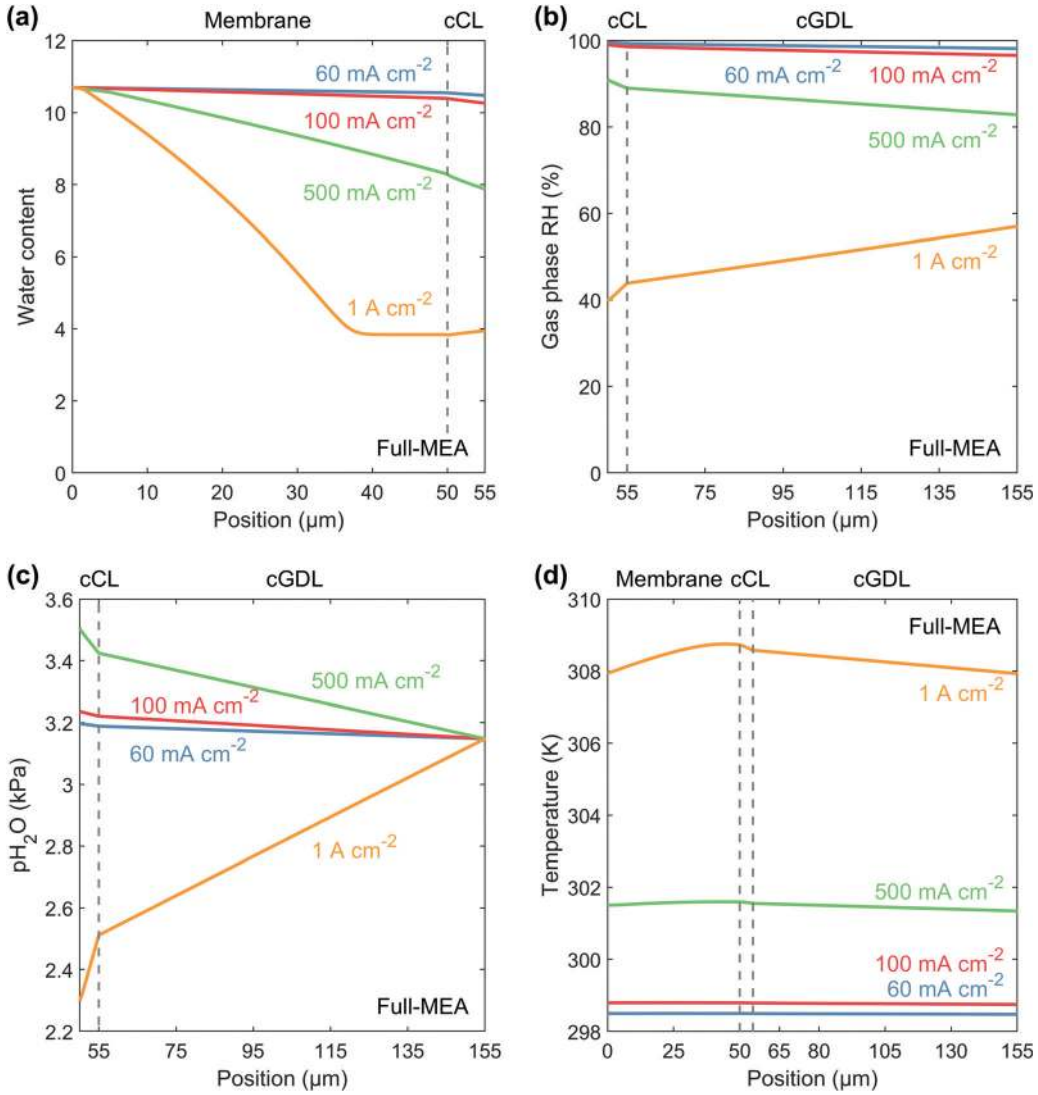

Fig. 5 (a) Water content in the membrane, (b) gas phase RH, (c) water partial pressure in the gas phase, and (d) the temperature for a full-MEA at 60, 100, 500, and 1000 mA cm^{-2}. The gas phase RH decreases with increasing current density because of the increase in vapor pressure as the cell heats up. Cathode feed composition is 97 mol% CO_2 and 3 mol% H_2O (water vapor pressure at 25 °C).

that is converted to CO) as a function of the TCD (Fig. 7a) is derived. More specifically,

$$\text{CO}_2\text{ consumption} = \frac{\text{Molar flowrate of CO}_2\text{ into the DM from the gas channel}}{\text{Inlet molar flowrate into the cell}}$$

and

$$\text{CO}_2\text{ conversion} = \frac{\text{CO partial current density converted to molar flowrate}}{\text{Inlet molar flowrate into the cell}}.$$

The CO_2 conversion for the three cases deviates slightly from each other at low TCD due to differences in the CO FE (not visible in figure), and eventually converges as CO FE approaches 100% for all three cases. At 100% CO FE, the CO_2 conversion scales linearly with the TCD (which is equal to the partial CO current density), as expected. CO_2 consumption is higher for the KOH exchange-MEA case at low TCD because CO_2 constantly reacts with the OH^- from the exchange solution, resulting in a lower CO_2 utilization efficiency (defined as the ratio of CO_2 conversion to consumption), shown in Fig. 7b. For the full-MEA and $KHCO_3$ exchange-MEA, since the membrane is in the HCO_3^- form (and does not consume CO_2 as the OH^- does) for TCD close to zero, the utilization efficiency starts at a higher value than that for a KOH exchange-MEA, and decreases with increasing TCD as more OH^- is produced. As the TCD increases, the OH^- concentration in the CL becomes comparable for a $KHCO_3$ exchange-MEA and a KOH exchange-MEA, but remains slightly lower for a full-MEA (Fig. 4b). The lower OH^- concentration in the full-MEA CL means less CO_2 consumption by homogeneous reactions, as shown in Fig. 7a, as well as a higher CO_2 utilization efficiency (Fig. 7b). The utilization efficiency for $KHCO_3$ exchange-MEA

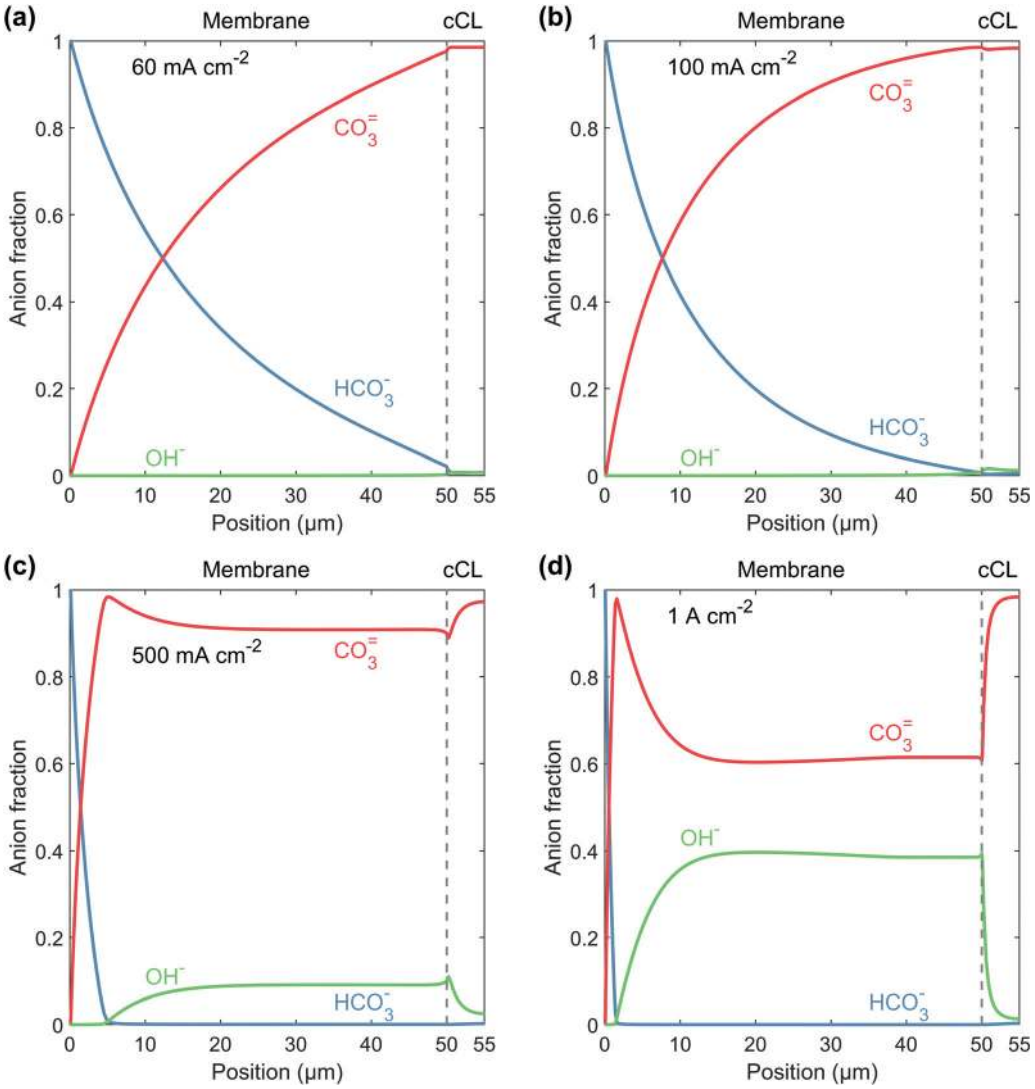

Fig. 6 Anion distribution in the membrane and cathode CL across a full-MEA cell at (a) 60 mA cm^{-2}, (b) 100 mA cm^{-2}, (c) 500 mA cm^{-2}, and (d) 1 A cm^{-2}. CO_2 is converted to $CO_3^{=}$ at the cathode by the OH^- produced from COER, transported as $CO_3^{=}$ to the anode, and released by the H^+ produced from OER. Cathode feed composition is 97 mol% CO_2 and 3 mol% H_2O.

and KOH exchange-MEA converges to 50% for TCD > 500 mA cm^{-2}, a result that can be explained by considering the stoichiometry of the electrochemical and homogeneous reactions, listed in Fig. 7c. The reaction stoichiometry also suggests a 1 : 2 O_2 to CO_2 ratio at the anode gas outlet, consistent with measurements by Liu *et al.*[68] To increase the utilization efficiency for exchange-MEAs, the consumption of CO_2 by OH^- needs to be reduced, which could be achieved by a lower rate coefficient for the homogeneous reaction of CO_2 and OH^- (Fig. S2, ESI†). However, this would also result in a more rapid pH change near the cathode, and a larger Nernstian overpotential. Understanding such tradeoffs is crucial to fine-tuning the cell design and maximizing efficiency.

In the model, the gas-channel composition is assumed to remain constant at the feed composition, which is valid only under conditions of low feed consumption (*e.g.*, high feed flowrate). Note that CO_2 concentration varies in the CL, and its profile is plotted in Fig. S1 (ESI†). In practice, however, CO_2 consumption can be as high 30% for a feed flowrate of 50 sccm and 1 A cm^{-2}, as shown above. This means that the gas composition in the cathode gas channel will vary based on the rate of consumption of CO_2 and H_2O, and the rate of production of CO and H_2. Assuming that the gas channel is well-mixed, we estimate its composition from a simple mass balance:

$$y_{GC,i} = \frac{N_{F,i} - N_{R,i}}{N_F - N_R} \quad (47)$$

where $y_{GC,i}$ is the mol fraction of gaseous species i in the gas channel; N_F and N_R are the total molar flowrate of the feed gas going into and out of the gas chamber into the GDL, respectively; $N_{F,i}$ and $N_{R,i}$ are the molar flowrate of species i in the feed gas going into and out of the gas chamber, respectively. Fig. 8 shows the resulting gas chamber composition for the full-MEA

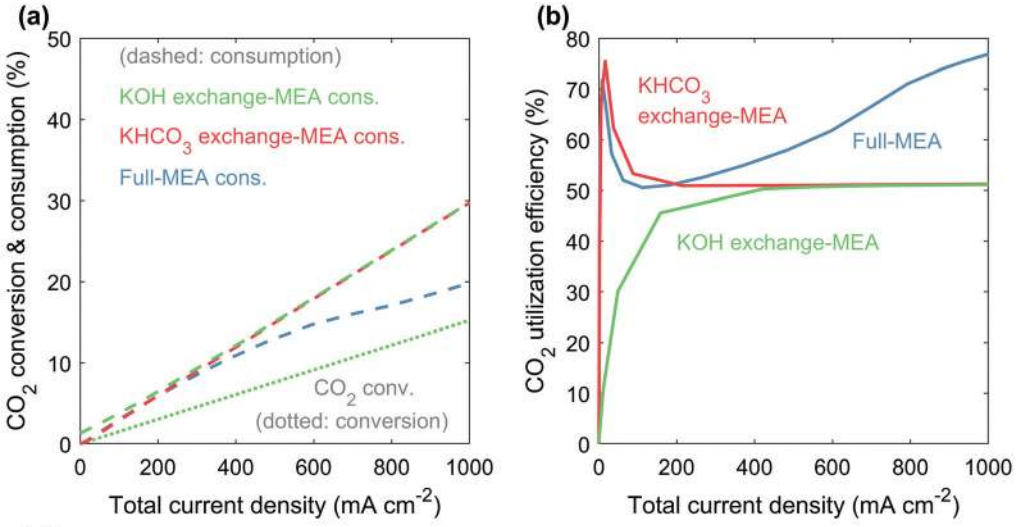

(c)

	Anode	Cathode
Charge transfer reaction	$2H_2O \rightarrow O_2 + 4H^+ + 4e^-$	$2CO_2 + 2H_2O + 4e^- \rightarrow 2CO + 4OH^-$
Homogeneous reactions	$2H^+ + 2CO_3^= \rightarrow 2HCO_3^-$	$2OH^- + 2CO_2 \rightarrow 2HCO_3^-$
near the electrode	$2H^+ + 2HCO_3^- \rightarrow 2H_2O + 2CO_2$	$2OH^- + 2HCO_3^- \rightarrow 2H_2O + 2CO_3^=$
Net reaction	$2CO_3^= \rightarrow O_2 + 2CO_2 + 4e^-$	$4CO_2 + 4e^- \rightarrow 2CO + 2CO_3^=$

Fig. 7 (a) CO_2 consumption (dotted) and conversion (dashed) calculated for a 50 sccm CO_2 feed at 100% RH (97 mol% CO_2, 3 mol% H_2O), room temperature. (b) CO_2 utilization efficiency defined as the fraction of CO_2 consumed that converts to CO. (c) Stoichiometric balance of the electrochemical and homogenous reactions across the cell showing only half of the CO_2 consumed is converted to CO.

(Fig. 8a) and the KOH exchange-MEA (Fig. 8b). At zero TCD, the gas composition in the cathode gas channel for the full-MEA is close to its feed composition since there are minimal reactions and crossover occurring. For the KOH exchange-MEA case, however, the CO_2 mole fraction is much lower than that in the feed (0.97) because CO_2 will be consumed by OH^- anions in the CL ionomer; the H_2O mole fraction is higher due to diffusion of H_2O from the anode chamber. The CO mole fraction increases steadily and the H_2 mole fraction is close to zero, as expected from the partial current densities. However,

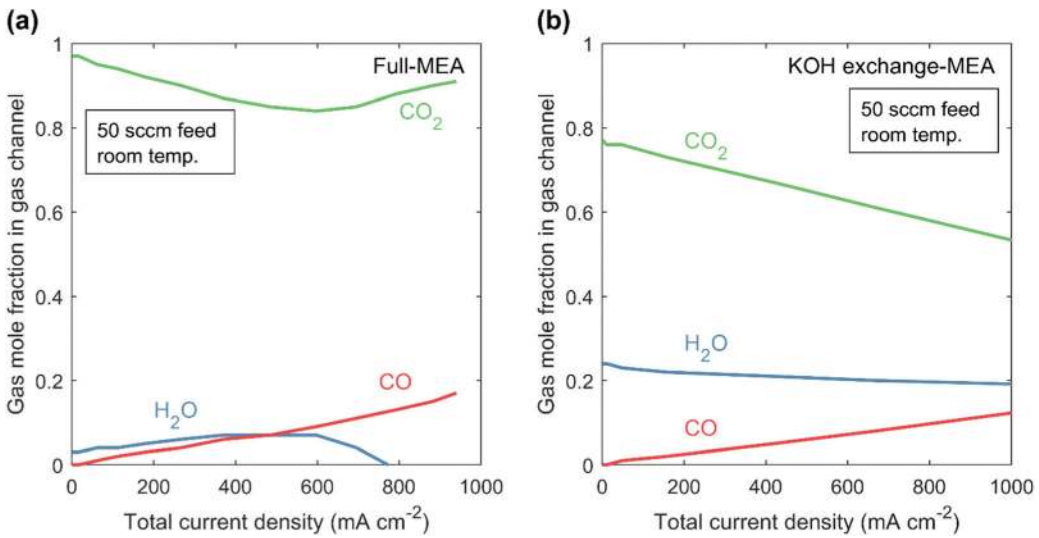

Fig. 8 Gas mol fraction in the cathode gas channel calculated assuming 50 sccm CO_2 feed with 100% RH (97 mol% CO_2, 3 mol% H_2O) at room temperature for (a) full-MEA and (b) KOH exchange-MEA. The vapor pressure at 298 K is 0.03 atm. Full-MEA becomes water-limited at approximately 750 mA cm^{-2}, and KOH-MEA is likely to be flooded.

two issues become apparent regarding water management. For the full-MEA, the H_2O mole fraction first increases slightly due to the temperature increase in the CL, as discussed in Fig. 5, and then drops to zero at approximately 750 mA cm^{-2}, indicating that the full-MEA becomes limited by the supply of water before it is limited by the supply of CO_2. On the other hand, the partial pressure for H_2O in the gas channel of the KOH exchange-MEA is significantly above its vapor pressure at ambient temperature ($\sim$0.03 atm), suggesting that flooding is likely to occur at the cathode GDE as water diffuses from the anode. Flooding in the cathode GDE will increase CO_2 mass-transport resistances significantly and decrease catalyst utilization.[37] Fig. 8 suggests a need for a higher-dimensional, integrated multiphase model to capture changes in the gas-channel composition, as well as additional physics to capture water condensation and multiphase flow in the GDE; studies of these effects are currently in progress.

Water management: temperature and membrane-thickness effects

To address issues concerning full-MEA dehydration and exchange-MEA flooding, we studied the effects of increasing the operating temperature and changing membrane thickness. In terms of the operating temperature, the water vapor pressure is $\sim$0.46 atm at 80 °C, compared to $\sim$0.03 atm at 25 °C. Thus, operating at 80 °C, a higher TCD can be achieved with more rapid kinetics (see eqn (35)), but the CO FE decreases below a cell potential of 3 V due to the lower solubility of CO_2 at elevated temperatures (Fig. 9a and b). The gas-channel composition shown in Fig. 9c also indicates that a current density of 1 A cm^{-2} lies below the CO_2- or H_2O-limited current densities

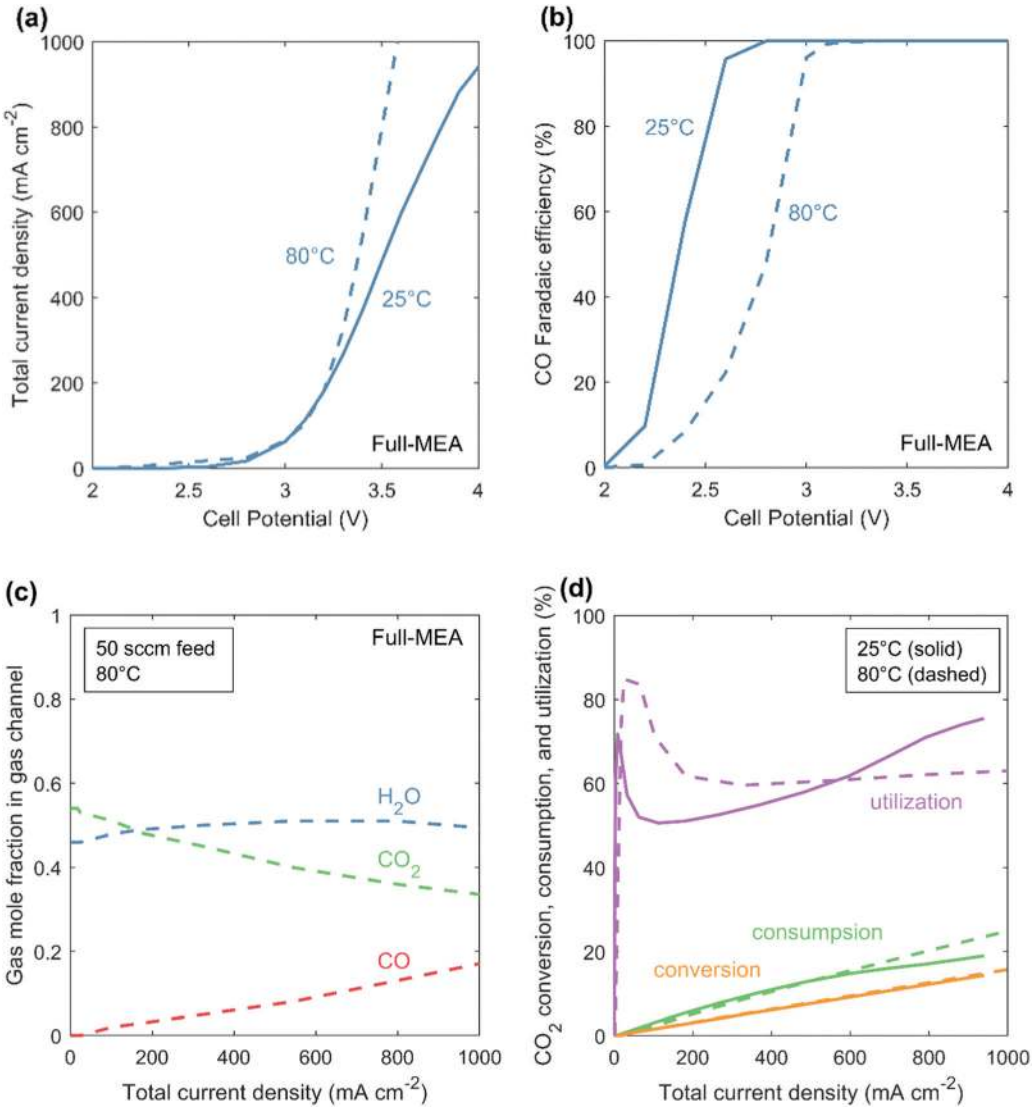

Fig. 9 (a) Total current density, (b) CO faradaic efficiency, (c) gas channel composition, and (d) CO_2 utilization analysis for a full-MEA at 80 °C with CO_2 feed at 100% RH (54 mol% CO_2, 46 mol% H_2O). Operating the cell at higher temperature increases the exchange current density, as well as water feed to the system. However, CO_2 solubility is compromised, resulting in lower CO faradaic efficiencies.

for a full-MEA. It should be noted that to obtain the same molar flowrate of CO_2 at 80 °C as at 25 °C for a feed flowrate of 50 sccm, the feed flowrate needs to be raised to 105 sccm in order to compensate for the higher vapor pressure of water. However, Fig. 9c shows that the full-MEA can operate up to 1 A cm^{-2} even at a third of the CO_2 molar flowrate provided at 80 °C. This observation reinforces our finding that the cell is operating in a low CO_2 utilization regime up to 1 A cm^{-2} at 50 sccm feed (Fig. 7).

The operating temperature can also affect CO_2 utilization, as it changes the reactions rates of electrochemical reactions and homogeneous reactions, as well as the equilibrium constants of the bicarbonate and water reactions. Since limited data is available for the buffer reaction rate constants in an ionomer, we show results assuming the same forward rate constants at 80 °C as at 25 °C for reactions (6)–(10). The equilibrium constant will vary based on eqn (11), as well as the reverse rate constant ($k_{-n} = k_n/K_n$). As shown in Fig. 9d, better CO_2 utilization can be achieved at higher temperatures when operating below approximately 600 mA cm^{-2} TCD, but the reverse is true when operating at higher TCDs. This effect is a consequence of increased diffusivity of ionic and neutral species, the shifted equilibria for reactions (6)–(10), and the relative rates of the homogeneous consumption of CO_2 and its electrochemical conversion at 80 °C. We note that the results shown here are based on the assumed temperature dependence of the various rate constants, which will vary based on the ionomer used. These results demonstrate the importance of studying homogenous reaction rates of the bicarbonate buffer system in different ionomer environments under various temperatures; manipulation of the bicarbonate buffer reaction rates is a potential route to increase CO_2 utilization of CO_2R systems.

Finally, as noted, one can also decrease the membrane thickness to help alleviate the dehydration issue in full-MEAs (although perhaps not the flooding issue in exchange-MEAs). Fig. 10 shows the effects of membrane thickness on the full-MEA performance. As expected, the TCD increases with a thinner membrane, with the difference becoming more significant with higher cell potentials due to both enhanced water transport as well as less ohmic losses, thereby reinforcing the finding that the full-MEA is ohmic-limited. Unlike changing temperature, the CO FE is not strongly impacted. Of course, decreasing the membrane thickness will result in increased crossover and worse CO_2 utilization. This is another tradeoff to consider, and is more prominent when producing aqueous products that have high solubility in the membrane.

Summary

A multiphysics model describing the effects of species transport, heat transfer, and the kinetics of all electrode and electrolyte reactions occurring in an MEA was developed and used to explore the electrochemical reduction of CO_2 to CO over Ag. As the current density rises above 100 mA cm^{-2}, MEAs become advantageous relative to planar cells containing an aqueous electrolyte or an aqueous GDL cell because they minimize the ohmic drop across the cell. Full-MEAs with gaseous feeds to both the anode and cathode gas channels can achieve a current density of 100 mA cm^{-2}, with approximately 40% reduction in the cell potential compared to an aqueous GDE cell, a consequence of their lower ohmic potential drop. However, such cells suffer from concentration polarization and membrane dehydration. Circulating an exchange solution through the anode channel enables an exchange-MEA to better maintain the local environment at the anode, and hydrate the membrane. With a KOH-exchange-solution feed, a reverse OH^- concentration gradient develops across the cell, lowering the thermodynamic potential that needs to be overcome. The alkaline environment created by KOH also suppresses the HER. For exchange-MEAs, cation transport

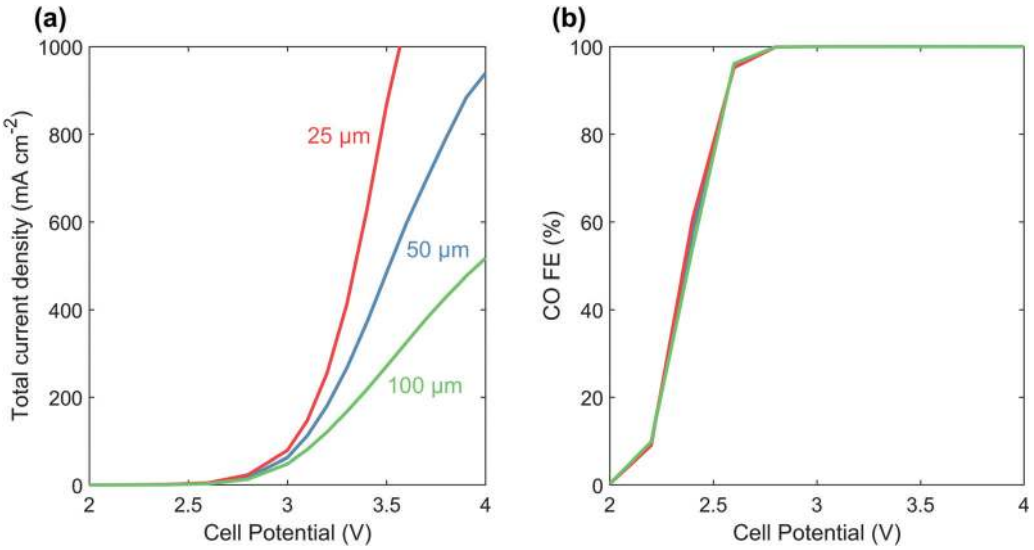

Fig. 10 (a) Total current density, (b) CO faradaic efficiency for the full-MEA case simulated with a 25 μm membrane (red), 50 μm membrane (base case, blue), and 100 μm membrane (green).

down the potential gradient limits the current density due to precipitation of the salt used in the exchange solution. It should also be noted that flooding is likely to occur in the cathode GDE of an exchange-MEA, as water diffuses from anode to cathode. High-temperature operation of a full-MEA allows introduction of more water vapor into the system, thereby overcoming the water limitations observed at room temperature; this also improves the charge transfer kinetics, although the reduction in CO_2 solubility and the changes in the homogeneous reaction rates and reaction equilibria can affect the CO FE and the CO_2 utilization efficiency of the cell. It is also possible to minimize flooding in an exchange-MEA by increasing the temperature at the cathode GDE in order to evaporate condensed water.

List of symbols

Roman

a_v	Specific surface area, m^{-1}
a_i	Activity of species i
A_k	Pre-exponential factor for reaction k, mA cm^{-2}
c_i	Concentration of species i, mol m^{-3}
D_i	Diffusivity of species i, m^2 s^{-1}
$E_{a,k}$	Activation energy for reaction k, kJ mol^{-1}
F	Faraday's constant, C mol^{-1}
H_i	Henry's constant of species i, M atm^{-1}
ΔH_n	Change of enthalpy for reaction n, kJ mol^{-1}
i_k	Current density for reaction k, mA cm^{-2}
i_l	Electrolyte current density, mA cm^{-2}
$i_{o,k}$	Exchange current density of reaction k, mA cm^{-2}
i_s	Electrode current density, mA cm^{-2}
IEC	Ion-exchange capacity, mmol g^{-1}
j_i	Diffusive mass flux of species i, g m^{-2} s^{-1}
k_n	Rate constant for homogeneous reaction n, s^{-1} or L mol^{-1} s^{-1}
$k_{T,m}$	Heat transfer coefficient of medium m, W m^{-1} K^{-1}
K_n	Equilibrium constant for reaction n
M_i	Molar mass of species i, g mol^{-1}
M_n	Average molar mass of gaseous mixture, g mol^{-1}
n_i	Mass flux of species i, g m^{-2} s^{-1}
n_k	Number of electrons transferred in reaction k
p_α	Total pressure in phase α, atm
p_{vap}	Vapor pressure, atm
q	Heat flux, J m^{-2}
q_l	Electrolyte flow rate, ml min^{-1}
$r_{p,m}$	Pore radius in medium m,
R	Gas constant, J mol^{-1} K^{-1}
$R_{\beta,i}$	Volumetric rate of reaction of species i from bulk reaction β, g m^{-3} s^{-1}
$s_{i,k}$	Stoichiometric coefficient of species i in reaction k
ΔS_n	Change of entropy for reaction n, J mol^{-1} K^{-1}
T	Temperature, K
u_β	Mass-averaged fluid velocity of fluid β, m s^{-1}
u_i	Mobility of species i, s mol kg^{-1}
U_k^o	Reference potential of reaction k, V
$v_{p,i}$	Diffusion volume of species i
V_i	Molar volume of species i, ml mol^{-1}
x_j	Mole fraction of aqueous species j
y_i	Mole fraction of gaseous species i
z_i	Charge of species i

Greek

α_k	Transfer coefficient of reaction k
γ_k	Reaction order of reaction k
δ_{TF}	Electrolyte thin film thickness
ε_m	Porosity of medium m
ζ_i	Species-water to species-membrane interaction ratio
η_k	Surface overpotential of reaction k, V
κ_m	Permeability of medium m, m^2
λ	Water content
μ_β	Viscosity of fluid β, Pa s
ξ	Electro-osmotic coefficient
ρ_i	Mass density of species i, g cm^{-3}
σ_m	Electronic conductivity in medium m, S m^{-1}
τ_m	Tortuosity of medium m
ϕ_α	Electric potential of phase α, V
ω_i	Mass fraction of species i
Π_k	Peltier coefficient of reaction k, V

Subscript

B	Bulk
CT	Charge transfer
g	Gaseous mixture
i	Gaseous species
j	Aqueous species
k	Reaction
l	Liquid phase
n	Homogeneous reaction number
p	Pore
PT	Phase transfer
s	Solid
TF	Electrolyte thin film
w	Water

Superscript

o	Intrinsic value or standard state
ref	Reference
eff	Effective
E	Electrolyte
K	Knudsen
m	Mass-averaged
M	Membrane

Acronyms

AEM	Anion-exchange membrane
CL	Catalyst layer
CO_2R	CO_2 reduction
COER	CO evolution reaction
CT	Charge transfer

DM	Diffusion medium
HER	H_2 evolution reaction
MEA	Membrane-electrode assembly
OER	Oxygen evolution reaction
RH	Relative humidity

Conflicts of interest

There are no conflicts to declare.

Acknowledgements

This material is based upon work performed by the Joint Center for Artificial Photosynthesis, a DOE Energy Innovation Hub, supported through the Office of Science of the U.S. Department of Energy under Award Number DE-SC0004993.

References

1 O. S. Bushuyev, P. De Luna, C. T. Dinh, L. Tao, G. Saur, J. van de Lagemaat, S. O. Kelley and E. H. Sargent, *Joule*, 2018, **2**, 825–832.
2 J. W. Ager and A. A. Lapkin, *Science*, 2018, **360**, 707–708.
3 S. Verma, B. Kim, H. R. Jhong, S. Ma and P. J. Kenis, *ChemSusChem*, 2016, **9**, 1972–1979.
4 D. Higgins, C. Hahn, C. X. Xiang, T. F. Jaramillo and A. Z. Weber, *ACS Energy Lett.*, 2019, **4**, 317–324.
5 R. L. Cook, R. C. Macduff and A. F. Sammells, *J. Electrochem. Soc.*, 1990, **137**, 607–608.
6 K. Hara and T. Sakata, *Bull. Chem. Soc. Jpn.*, 1997, **70**, 571–576.
7 K. Hara, N. Sonoyama and T. Sakata, *Stud. Surf. Sci. Catal.*, 1998, **114**, 577–580.
8 K. Ogura, H. Yano and F. Shirai, *J. Electrochem. Soc.*, 2003, **150**, D163–D168.
9 S. Ma, R. Luo, S. Moniri, Y. C. Lan and P. J. A. Kenis, *J. Electrochem. Soc.*, 2014, **161**, F1124–F1131.
10 S. Verma, X. Lu, S. Ma, R. I. Masel and P. J. Kenis, *Phys. Chem. Chem. Phys.*, 2016, **18**, 7075–7084.
11 C. T. Dinh, T. Burdyny, M. G. Kibria, A. Seifitokaldani, C. M. Gabardo, F. P. G. de Arquer, A. Kiani, J. P. Edwards, P. De Luna, O. S. Bushuyev, C. Q. Zou, R. Quintero-Bermudez, Y. J. Pang, D. Sinton and E. H. Sargent, *Science*, 2018, **360**, 783–787.
12 D. M. Weekes, D. A. Salvatore, A. Reyes, A. Huang and C. P. Berlinguette, *Acc. Chem. Res.*, 2018, **51**, 910–918.
13 B. Endrodi, G. Bencsik, F. Darvas, R. Jones, K. Rajeshwar and C. Janaky, *Prog. Energy Combust. Sci.*, 2017, **62**, 133–154.
14 S. Gottesfeld, D. R. Dekel, M. Page, C. Bae, Y. Yan, P. Zelenay and Y. S. Kim, *J. Power Sources*, 2018, **375**, 170–184.
15 N. R. d. Tacconi, W. Chanmanee, B. H. Dennis and K. Rajeshwar, *J. Mater. Res.*, 2017, **32**, 1727–1734.
16 R. L. Cook, R. C. Macduff and A. F. Sammells, *J. Electrochem. Soc.*, 1988, **135**, 1470–1471.
17 Y. Hori, H. Ito, K. Okano, K. Nagasu and S. Sato, *Electrochim. Acta*, 2003, **48**, 2651–2657.
18 C. Delacourt, P. L. Ridgway, J. B. Kerr and J. Newman, *J. Electrochem. Soc.*, 2008, **155**, B42–B49.
19 D. A. Salvatore, D. M. Weekes, J. He, K. E. Dettelbach, Y. C. Li, T. E. Mallouk and C. P. Berlinguette, *ACS Energy Lett.*, 2017, **3**, 149–154.
20 S. R. Narayanan, B. Haines, J. Soler and T. I. Valdez, *J. Electrochem. Soc.*, 2011, **158**, A167–A173.
21 Y. C. Li, D. Zhou, Z. Yan, R. H. Gonçalves, D. A. Salvatore, C. P. Berlinguette and T. E. Mallouk, *ACS Energy Lett.*, 2016, **1**, 1149–1153.
22 S. M. A. Kriescher, K. Kugler, S. S. Hosseiny, Y. Gendel and M. Wessling, *Electrochem. Commun.*, 2015, **50**, 64–68.
23 G. Wang, J. Pan, S. P. Jiang and H. Yang, *J. CO_2 Util.*, 2018, **23**, 152–158.
24 M. Ni, *J. Power Sources*, 2012, **202**, 209–216.
25 V. Menon, Q. X. Fu, V. M. Janardhanan and O. Deutschmann, *J. Power Sources*, 2015, **274**, 768–781.
26 J. Rosen, G. S. Hutchings, Q. Lu, S. Rivera, Y. Zhou, D. G. Vlachos and F. Jiao, *ACS Catal.*, 2015, **5**, 4293–4299.
27 M. Ma, K. Liu, J. Shen, R. Kas and W. A. Smith, *ACS Energy Lett.*, 2018, **3**, 1301–1306.
28 J. Shen, R. Kortlever, R. Kas, Y. Y. Birdja, O. Diaz-Morales, Y. Kwon, I. Ledezma-Yanez, K. J. Schouten, G. Mul and M. T. Koper, *Nat. Commun.*, 2015, **6**, 8177.
29 J. Peng, A. L. Roy, S. G. Greenbaum and T. A. Zawodzinski, *J. Power Sources*, 2018, **380**, 64–75.
30 Y. S. Li, T. S. Zhao and W. W. Yang, *Int. J. Hydrogen Energy*, 2010, **35**, 5656–5665.
31 Q. Duan, S. Ge and C.-Y. Wang, *J. Power Sources*, 2013, **243**, 773–778.
32 K. G. Schulz, U. Riebesell, B. Rost, S. Thoms and R. E. Zeebe, *Mar. Chem.*, 2006, **100**, 53–65.
33 A. G. Divekar, A. M. Park, Z. R. Owczarczyk, S. Seifert, B. S. Pivovar and A. M. Herring, *ECS Trans.*, 2017, **80**, 1005–1011.
34 D. B. Spry and M. D. Fayer, *J. Phys. Chem. B*, 2009, **113**, 10210–10221.
35 S. J. Sondheimer, N. J. Bunce, M. E. Lemke and C. A. Fyfe, *Macromolecules*, 1986, **19**, 339–343.
36 F. C. Cetinbas, R. K. Ahluwalia, N. Kariuki, V. De Andrade, D. Fongalland, L. Smith, J. Sharman, P. Ferreira, S. Rasouli and D. J. Myers, *J. Power Sources*, 2017, **344**, 62–73.
37 L. C. Weng, A. T. Bell and A. Z. Weber, *Phys. Chem. Chem. Phys.*, 2018, **20**, 16973–16984.
38 A. El-Kharouf, T. J. Mason, D. J. L. Brett and B. G. Pollet, *J. Power Sources*, 2012, **218**, 393–404.
39 C. Y. Du, P. F. Shi, X. Q. Cheng and G. P. Yin, *Electrochem. Commun.*, 2004, **6**, 435–440.
40 I. V. Zenyuk, E. Medici, J. Allen and A. Z. Weber, *Int. J. Hydrogen Energy*, 2015, **40**, 16831–16845.
41 A. Z. Weber and J. Newman, *J. Electrochem. Soc.*, 2006, **153**, A2205–A2214.
42 S. Thiele, T. Fürstenhaupt, D. Banham, T. Hutzenlaub, V. Birss, C. Ziegler and R. Zengerle, *J. Power Sources*, 2013, **228**, 185–192.

43 E. N. Fuller, P. D. Schettle and J. C. Giddings, *Ind. Eng. Chem.*, 1966, **58**, 18–27.
44 *CRC handbook of chemistry and physics*, CRC Press, Cleveland, Ohio, 1977.
45 N. A. Lange and J. G. Speight, *Lange's handbook of chemistry*, McGraw-Hill, New York, 16th edn, 2005.
46 T. S. Light, S. Licht, A. C. Bevilacqua and K. R. Morash, *Electrochem. Solid-State Lett.*, 2005, **8**, E16–E19.
47 R. E. Zeebe, *Geochim. Cosmochim. Acta*, 2011, **75**, 2483–2498.
48 J. S. Newman and K. E. Thomas-Alyea, *Electrochemical systems*, J. Wiley, Hoboken, N.J., 3rd edn, 2004.
49 W. Sheng, Z. Zhuang, M. Gao, J. Zheng, J. G. Chen and Y. Yan, *Nat. Commun.*, 2015, **6**, 5848.
50 W. Sheng, M. Myint, J. G. G. Chen and Y. S. Yan, *Energy Environ. Sci.*, 2013, **6**, 1509–1512.
51 W. Sheng, H. A. Gasteiger and Y. Shao-Horn, *J. Electrochem. Soc.*, 2010, **157**, B1529–B1536.
52 J. Durst, A. Siebel, C. Simon, F. Hasché, J. Herranz and H. A. Gasteiger, *Energy Environ. Sci.*, 2014, **7**, 2255–2260.
53 J. Durst, C. Simon, F. Hasche and H. A. Gasteiger, *J. Electrochem. Soc.*, 2014, **162**, F190–F203.
54 J. Zheng, W. Sheng, Z. Zhuang, B. Xu and Y. Yan, *Sci. Adv.*, 2016, **2**, e1501602.
55 T. Cheng, L. Wang, B. V. Merinov and W. A. Goddard, 3rd, *J. Am. Chem. Soc.*, 2018, **140**, 7787–7790.
56 D. Y. Kuo, J. K. Kawasaki, J. N. Nelson, J. Kloppenburg, G. Hautier, K. M. Shen, D. G. Schlom and J. Suntivich, *J. Am. Chem. Soc.*, 2017, **139**, 3473–3479.
57 E. Nurlaela, T. Shinagawa, M. Qureshi, D. S. Dhawale and K. Takanabe, *ACS Catal.*, 2016, **6**, 1713–1722.
58 L. Giordano, B. Han, M. Risch, W. T. Hong, R. R. Rao, K. A. Stoerzinger and Y. Shao-Horn, *Catal. Today*, 2016, **262**, 2–10.
59 T. Hatsukade, K. P. Kuhl, E. R. Cave, D. N. Abram and T. F. Jaramillo, *Phys. Chem. Chem. Phys.*, 2014, **16**, 13814–13819.
60 T. A. Zawodzinski, J. Davey, J. Valerio and S. Gottesfeld, *Electrochim. Acta*, 1995, **40**, 297–302.
61 X. H. Wang, J. P. McClure and P. S. Fedkiw, *Electrochim. Acta*, 2012, **79**, 126–132.
62 T. Yamanaka, T. Takeguchi, H. Takahashi and W. Ueda, *J. Electrochem. Soc.*, 2009, **156**, B831–B835.
63 K. N. Grew, X. M. Ren and D. Chu, *Electrochem. Solid-State Lett.*, 2011, **14**, B127–B131.
64 K. N. Grew and W. K. S. Chiu, *J. Electrochem. Soc.*, 2010, **157**, B327–B337.
65 P. Choi, N. H. Jalani and R. Datta, *J. Electrochem. Soc.*, 2005, **152**, E123–E130.
66 C. C. McCrory, S. Jung, J. C. Peters and T. F. Jaramillo, *J. Am. Chem. Soc.*, 2013, **135**, 16977–16987.
67 H. Yanagi and K. Fukuta, *ECS Trans.*, 2008, **16**, 257–262.
68 Z. C. Liu, H. Z. Yang, R. Kutz and R. I. Masel, *J. Electrochem. Soc.*, 2018, **165**, J3371–J3377.
69 A. Patru, T. Binninger, B. Pribyl and T. J. Schmidt, *J. Electrochem. Soc.*, 2019, **166**, F34–F43.
70 H.-S. Shiau, I. V. Zenyuk and A. Z. Weber, *J. Electrochem. Soc.*, 2017, **164**, E3583–E3591.

